Materials Advances

ROYAL SOCIETY OF CHEMISTRY

PAPER

View Article Online
View Journal | View Issue

Cite this: *Mater. Adv.*, 2024, 5, 8455

Characteristics of Ag-doped $LaMnO_3$ perovskite oxide and its application as a solid oxide fuel cell cathode†

Akihiro Takamatsu,[a] Masatsugu Oishi,*[a] Shinpei Goda,[a] Hiroki Takemura,[a] Konosuke Mitsushio,[a] Satoshi Sugano,[a] Takashi Yamamoto,[a] Toshiaki Ina,[b] Haruo Kishimoto[c] and Takaaki Sakai*[c]

Received 24th February 2024,
Accepted 2nd September 2024

DOI: 10.1039/d4ma00190g

rsc.li/materials-advances

Ag-doped $LaMnO_3$ perovskite oxides were synthesized as new cathode materials for solid oxide fuel cells (SOFCs), and their phase stability, reactivity with yttria-stabilized zirconia (YSZ), electronic state of Mn, electrical conductivity, and power generation properties were investigated. $La_{0.9}Ag_{0.1}MnO_{3\pm\delta}$ (LAM01) showed no evidence of Ag metal deposition, whereas $La_{0.9}Ag_{0.2}MnO_{3\pm\delta}$ (LAM02) showed Ag metal deposition, suggesting that Ag dissolved in a perovskite-type structure and its solid solution limit for the La-site was 10%. LAM01 did not react with the YSZ electrolyte at 975 °C for 100 h. The electronic state of Mn was between that of the trivalent and tetravalent states at room temperature, suggesting that the Ag acceptor dopant was charge-compensated by the oxidation of Mn. Electrical conductivity and Seebeck coefficient measurements indicated that the main charge carrier was electron–hole. Stable power generation properties were obtained using the LAM01 cathode and indicated that the Ag acceptor was stable and was compatible with the YSZ electrolyte. Therefore, Ag-doped $LaMnO_3$ is promising as a novel SOFC cathode.

1. Introduction

Solid oxide fuel cells (SOFCs) have attracted much attention in recent years due to their high power generation efficiency.[1–5] Yttria-stabilized zirconia (8 mol% Y_2O_3–ZrO_2; YSZ) is widely used as an electrolyte in SOFCs because of its excellent performance, low cost, and material stability.[6–8] In a conventional SOFC cell, a Ni/YSZ cermet is used for the anode[1–3] and a metal oxide, such as (La, Sr)$CoO_{3-\delta}$ (LSC),[9–13] (La, Sr)$MnO_{3-\delta}$ (LSM),[13–15] and $La_{1-x}Sr_xCo_{1-y}Fe_yO_{3-\delta}$ (LSCF),[16–19] is used for the cathodes. However, a challenge in SOFCs with an YSZ electrolyte is the formation of a high-resistance reaction phase between the electrolyte and the cathode; when LSC or LSCF, which has high catalytic activity, is used, the A-site element reacts with Zr in the electrolyte. In particular, the A-site element Sr reacts with ZrO_2 to form $SrZrO_3$, which has low oxide ion conductivity, leading to a large increase in the ohmic resistance of the SOFC cell.[20–23] An interlayer, such as $Ce_{0.9}Gd_{0.1}O_{2-\delta}$ (GDC), can be introduced between these cathode materials and YSZ, but the formation of $SrZrO_3$ cannot be prevented completely.[24] Another problem emerges from the introduction of a GDC interlayer; GDC and YSZ have the same fluorite structures, and thus they easily react, resulting in the formation of a CeO_2–ZrO_2 solid solution with low oxide ion conductivity.[25] Mn-type perovskite oxides as cathodes have been proposed as a solution to this problem because of their higher chemical compatibility with the YSZ electrolyte than Co-type perovskite oxides. Yokokawa *et al.*[21] reported that chemical thermodynamic considerations showed that the A-site elements are unlikely to react with ZrO_2 in the $LaMnO_3$ system, and Chen *et al.*[26] also reported that Sr in $La_{1-x}Sr_xMnO_{3\pm\delta}$ does not react under cathode baking conditions. However, $LaMnO_3$-based materials also form $SrZrO_3$ under a low-oxygen atmosphere;[26,27] during SOFC operation, the cathode side reaches a low oxygen partial pressure depending on the electrode overpotential. Therefore, even if $SrZrO_3$ is not formed during the electrode sintering, it will eventually be formed during the SOFC operation. The formation of a high-resistance reaction phase has also been reported for Ca^{2+}-doped materials;[28] thus, using alkaline earth metal elements as dopants, which are essential for

[a] *Graduate School of Technology, Industrial and Social Science, Tokushima University, 2-1 Minami Josanjima Cho, Tokushima 770-8506, Japan. E-mail: ooishi.masatsugu@tokushima-u.ac.jp*
[b] *Japan Synchrotron Radiation Research Institute (JASRI), 1–1–1 Kouto, Sayo-cho, Sayo-gun, Hyogo 679–5198, Japan*
[c] *National Institute of Advanced Industrial Science and Technology (AIST), Global Zero Emission Research Center, 16-1 Onogawa, Tsukuba, Ibaraki 305-8569, Japan. E-mail: sakai-takaaki@aist.go.jp; Tel: +81-29-861-8212*

† Electronic supplementary information (ESI) available. See DOI: https://doi.org/10.1039/d4ma00190g

increasing electrode activity, results in the formation of a $ReZrO_3$-based high-resistance phase.

To overcome this problem, we are investigating noble dopants other than alkaline earth metal elements. Ag has been selected as a candidate noble dopant, and Ag-doped $LaMnO_3$ materials have been investigated for potential applications including magnetic memory devices, and magnetic field sensors, and their thermoelectric and magnetic properties have been studied.[29,30] In the SOFC cathode, Ag is not expected to react with ZrO_2 or Y_2O_3. Ag is used as a catalyst and current collector in SOFC systems,[31–35] and exsolved Ag nanocatalysts on perovskite-type oxides have been reported. Kim *et al.*[35] evaluated the catalytic properties of Ag on $BaCoO_3$[35] and Sažinas *et al.*[31] evaluated them on $LaSrMnO_{3-\delta}$. In these studies, the exsolution of Ag nanoparticles was caused by annealing in a hydrogen atmosphere from 300 to 600 °C. Thus, Ag does not interfere with the electrode reaction even if it is precipitated.

In the present study, which also uses Ag, the catalytic properties of Ag metal are not the target. We focused on Ag as the acceptor dopant and evaluated the Ag-doped $LaMnO_3$ materials as the cathodes for SOFCs. The cathode properties of $LaMnO_3$ materials were evaluated using Ag as a low-valence element doped into the A-site of perovskite-type oxides to search for an alternative acceptor-dopant to alkaline earth metals. Ag-doped $LaMnO_3$ was synthesized by using the sol–gel method, and its electrical conductivity, Seebeck coefficient, and electronic structure were investigated. Finally, Ag-doped $LaMnO_3$ was used as a SOFC cathode, and its performance was measured.

2. Experimental section

2.1 Sample preparation

The sol–gel method was used to synthesize 10 mol% Ag-doped $LaMnO_3$ ($La_{0.9}Ag_{0.1}MnO_{3\pm\delta}$, LAM01) and 20 mol% Ag-doped $LaMnO_3$ ($La_{0.8}Ag_{0.2}MnO_{3\pm\delta}$, LAM02) from La $(NO_3)_3{\cdot}6H_2O$ (99.9%, FUJIFILM Wako Pure Chemical Corp.), $AgNO_3$ (99.8%, FUJIFILM Wako Pure Chemical Corp.), $Mn(NO_3)_2{\cdot}6H_2O$ (99.9%, FUJIFILM Wako Pure Chemical Corp.), and citric acid monohydrate.[36] The starting materials were dissolved in distilled water at a molar ratio of 0.9 : 0.1 : 1 : 2 and 0.8 : 0.2 : 1 : 2, were stirred with a hot stirrer until the water was fully evaporated, and the resulting precursor was calcined at 400 °C for 1 h in air, mixed in a mortar, and sintered at 925 °C for 2 h. $La_{0.9}Sr_{0.1}MnO_{3\pm\delta}$ (LSM01) was prepared in a similar way using $Sr(NO_3)_2$ (98%–102%, FUJIFILM Wako Pure Chemical Corp.) as the Sr source. The crystal structures of the powders and annealed powders were evaluated using X-ray diffraction (XRD; Miniflex600 or Smart Lab, Rigaku Corp.) with Cu Kα radiation at room temperature.

2.2 Characterization

For *in situ* X-ray absorption fine structure (XAFS) measurements, the samples were mixed with boron nitride and adjusted to a suitable concentration for the XAFS transmission method. In the experiment, the sample was placed in an electric furnace installed at the beamline, and the temperature was increased at the rate of 10 °C min^{-1} up to 800 °C in O_2 gas. O_2 gas was continuously supplied at 60 cc min^{-1} during the measurements. The *in situ* XAFS measurements of the Mn K-edges were performed at beamline BL01B1 at SPring-8 (Hyogo, Japan) using a transmission ionization chamber and Si (111) double-crystal monochromator.[37] The energy scale was calibrated using a Cu foil. Ag K-edge X-ray absorption near edge absorption structure (XANES) was measured using a laboratory-type spectrometer (R-XAS Looper, Rigaku Corp.) operated in transmission mode at room temperature using Ge(840) monochromator crystals.[38] The Mn K-edge XANES and extended X-ray absorption fine structure (EXAFS) spectra were analyzed *via* the IFEFFIT program code using ATHENA.[39] For Ag K-edge XANES, background removal and normalization of an X-ray absorption spectrum were performed using a self-made macro programmed using Igor Pro 6 (WaveMatrics, USA) by Yamamoto *et al.*[40]

An electrolyte-supported cell was fabricated for the power generation test. Electrolyte pellets 0.3 mm thick were prepared by sintering 8YSZ (TZ-8Y, Tosoh Corp.) at 1500 °C for 10 h. The anode was prepared by mixing NiO and YSZ in a ratio of 7 : 3 wt%. The anode was screen-printed on the 8YSZ pellet and sintered at 1400 °C for 5 h. $LaMnO_3$ powder was used for the cathode. The electrode powders were mixed with ethylcellulose (Kishida Chemical Co., Ltd) and a thinner to form a paste. The cathode paste was also screen-printed, 80 mesh Pt current collectors were attached to the anode and cathode, and then the cell was sandwiched with Pyrex glass sealing rings and heated at 925 or 1000 °C for 1 h to sinter the cathode before the power generation tests. For the power generation tests, humidified H_2 with $P(H_2O)$ = 2.3% gas and dry O_2 gas were introduced into the anode and cathode compartments, respectively, at a flow rate of 100 cc min^{-1}. The electrochemical properties were evaluated using an electrochemical impedance analyzer (HZ-Pro, Meiden Hokuto Denko Corp.), and a potentiostat/galvanostat (HA-151B, Meiden Hokuto Denko Corp.). The electric conductivity was measured using a standard AC four-terminal method (IM3590, Hioki Corp.). The thermoelectric power was measured following the electrical conductivity measurement by using the outer two electrodes of the four-probe conductivity bar for temperatures ranging from 300 to 900 °C in air. The temperature gradients were applied by flowing the air to one side of the sample. Electromotive force across the sample bar was measured with a nanovoltmeter (Keithley 2182A/J, Tektronix, Inc.). The Seebeck coefficient of the specimen was determined from the electromotive force slope and temperature difference after compensation for the thermoelectric power of Pt.[41,42]

Powder morphology was observed by scanning electron microscopy (SEM; JSM-6510A, JEOL Ltd) and field emission-SEM (S-4700, Hitachi High-Tech Corp.). Selected area electron diffraction patterns and field emission-TEM observations (JEM-2100F, JEOL Ltd) were used to obtain high-angle annular dark field-scanning transmission electron microscopy (HAADF-STEM) images. Energy dispersive X-ray spectrometry (EDX) was used to determine the elemental composition of individual particles. X-ray

photoelectron spectroscopy (XPS) was performed on a photoelectron spectrometer (PHI5000 Versa Probe II, ULVAC-PHI Inc.) with monochromatized Al–K radiation (1486.6 eV).

3. Results and discussion

3.1 Crystal structure, stability of the Ag dopant, and compatibility with the electrolyte

Fig. 1(a) shows XRD profiles of the LAM01 and LAM02 samples. For comparison, XRD profile of undoped $LaMnO_3$ is also shown. The XRD profile of LAM01 revealed peaks that were all attributed to the $LaMnO_3$ perovskite, which has a trigonal structure (space group: $R\bar{3}c$, No. 167). The XRD profile of LAM02 was also mainly attributed to the $LaMnO_3$ perovskite, but a small peak was observed at around 38° that corresponded to the main peak of Ag. Rietveld refinements were conducted for LAM01 and LAM02 XRD profiles with the trigonal ($R\bar{3}c$) structure (Fig. S1 and Table S1, ESI†). The lattice constants of LAM01 and LAM02 were similar, indicating that the state of the solved Ag in the $LaMnO_3$ structure of LAM01 and LAM02 was also similar. SEM images showed that LAM01 and LAM02 were micron-sized powders (Fig. 2). However, the LAM02 powders had nanosized particles on the surface of the micron-sized particles in Fig. 2, suggesting the Ag particles were deposited in LAM02. Hence, the solution limit of Ag in the La-site of $LaMnO_3$ was ~10%.

To examine the stability of doped Ag, LAM01 powder was annealed at 975 °C for 100 h in air (Fig. 1(b)). The XRD peaks shifted slightly to a lower angle, suggesting that lattice expansion occurred in the annealed samples, and thus that reductive expansion occurred due to the formation of oxygen vacancies. However, the XRD profiles before and after annealing treatment were the same, and the Ag main peak at 38° was not observed after annealing. In addition, the SEM image showed no Ag metal deposition and the Ag atomic ratio of the LAM01 powder showed no major change after annealing treatment (Fig. 3(a) and Fig. S2, and Table 1 and S2, ESI†). Therefore, decomposition of LAM01 or deposition of Ag was not observed after annealing at 975 °C. In addition, the compatibility of LAM01 and 8YSZ was evaluated by mixing LAM01 and 8YSZ powders at a weight ratio of 1 : 1, forming them into φ10 mm pellets, and annealing at 975 °C for 100 h in air. The XRD profiles after annealing (Fig. 1(b)) were identical to those after annealing and no additional peaks due to the reaction of LAM01 and 8YSZ were identified. In addition, Fig. 3(b) shows

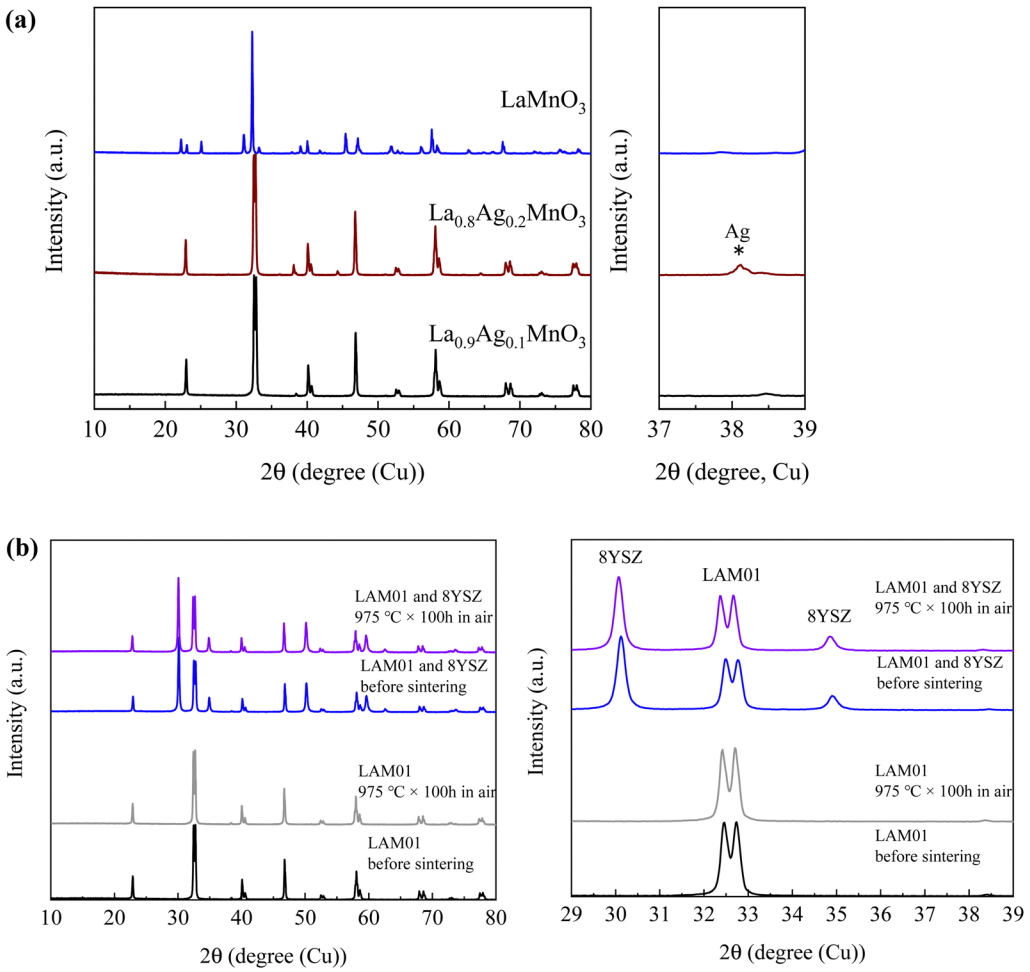

Fig. 1 XRD profiles of (a) Ag- and undoped $LaMnO_3$ and (b) LAM01 powder and mixed powder of LAM01 and 8YSZ before and after annealing at 975 °C.

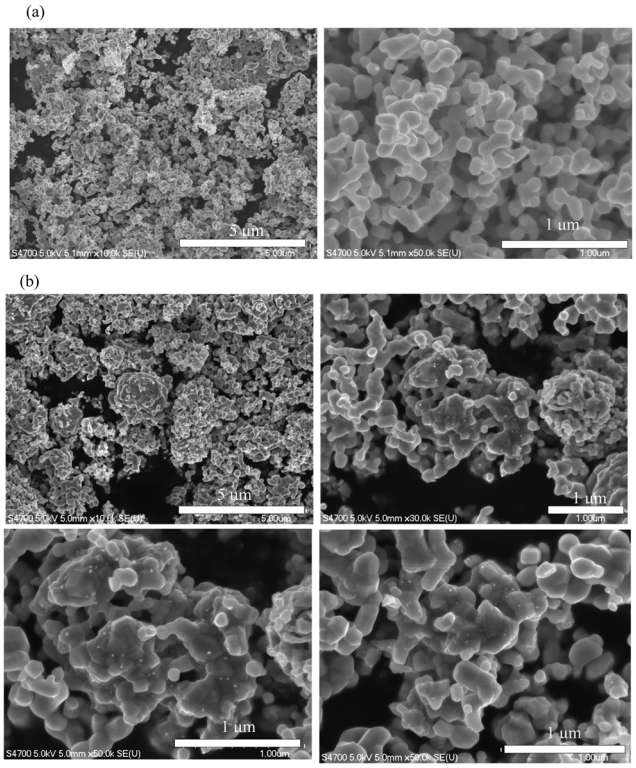

Fig. 2 SEM images of (a) LAM01 and (b) LAM02 pristine powders.

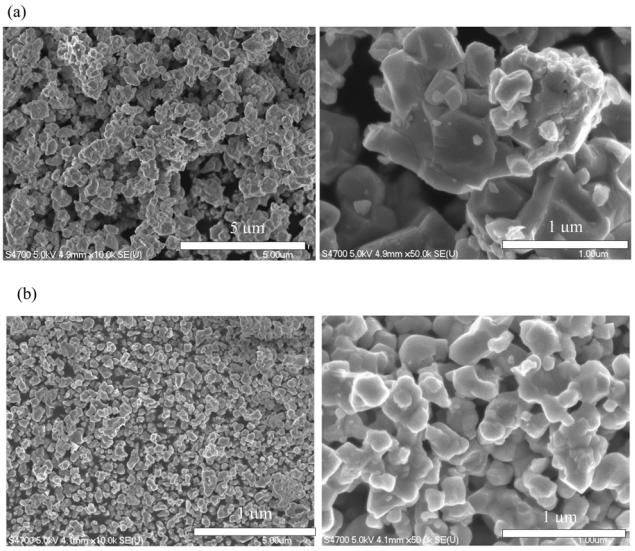

Fig. 3 SEM images of (a) LAM01 pristine powders annealed at 975 °C for 100 h in air and (b) LAM01 and 8YSZ powders mixed at a weight ratio of 1 : 1 and annealed at 975 °C for 100 h in air.

no Ag metal deposition after annealing. This indicates that LAM01 is compatible with 8YSZ below 975 °C.

3.2 Electronic and local structures

The Mn K-edge XANES spectrum of LAM01 measured at room temperature, the spectra of MnO, $LaMnO_3$ annealed in an N_2 atmosphere, and $CaMnO_3$ as references for the Mn^{2+}, Mn^{3+}, and Mn^{4+} states, respectively, are shown in Fig. 4(a). The $CaMnO_3$ (Mn^{4+}) reference sample has the orthorhombic perovskite structure (*Pnma*), and the $LaMnO_3$ (Mn^{3+}) reference sample has the orthorhombic perovskite structure (*Pbnm*), in which the MnO_6 octahedron is distorted by the Jahn–Teller effect. $LaMnO_3$ shows a stoichiometric composition at an oxygen partial pressure of 10^{-4} atm, whereas it shows an oxygen-rich composition in air.[43] Hence, $LaMnO_3$ annealed in an N_2 atmosphere at 1200 °C was used as the reference spectrum for Mn^{3+}. For the divalent ion reference, MnO (Mn^{2+}) with a cubic structure ($Fm\bar{3}m$) was used because a material with a similar local structure could not be obtained. Although the symmetry around Mn is different, the absorption edge shifts to a lower photon energy as the Mn is reduced. The absorption edge energy of LAM01 was higher than that of $LaMnO_3$, which suggested that the valence state of Mn was higher than the trivalent state but lower than the tetravalent state. Assuming La^{3+}, Ag^{1+}, and O^{2-} states, the valence state of Mn for the stoichiometric LAM01 was $Mn^{3.2+}$. This state was consistent with the results of Mn K-edge XANES spectra. Therefore, the acceptor Ag^{1+} dopant was charge-compensated by the oxidation of Mn, and oxygen vacancies were not formed or were negligible at room temperature. Fig. 4(b) shows the Ag K-edge XANES spectra of LAM01 together with the reference samples of Ag foil and Ag_2O. The Ag K-edge energy shifts to lower energy corresponding to the $Ag^0 \rightarrow Ag^+$ oxidation state change (Fig. 4(b) inset).[44,45] The XANES spectrum of LAM01 was different from that of Ag foil, which implies that Ag ions were doped in LAM01. The different XANES spectrum compared to Ag_2O suggests that the local structure around Ag ion in LAM01 is different from that around the Ag_2O reference sample.[46]

Table 1 EDX atomic concentrations of LAM01 measured by SEM-EDX

	La (at%)	Ag (at%)	Mn (at%)
Pristine powder	48.5	3.3	48.2
Powder annealed at 975 °C for 100 h	48.6	3.5	47.9

Fig. 4(c) shows the *in situ* Mn K-edge XANES spectra for LAM01 in a 100% O_2 atmosphere from room temperature to 800 °C. The Mn K-edge spectra changed continuously with isosbestic points, indicating the variations of the electronic structure at elevated temperatures. Fig. 4(d) shows the amplitudes of the Fourier transforms $\chi(R)$ obtained from k^3-weighted EXAFS oscillations of LAM01. The FT peak of the first coordination shell changed with temperature, suggesting a change in the MnO_6 octahedron symmetry. The decrease in the peak intensity at ~1.5 Å suggests a decrease in the CN around the Mn ions, a distortion in the MnO_6 octahedron symmetry, or both due to O desorption at the elevated temperature. In addition, the peak shifted to a longer distance above 500 °C. It implies the reductive expansion of LAM01 at elevated temperatures. Therefore, the symmetry around Mn in LAM01 changed with increasing temperature, and the concentration of oxygen defects increased at SOFC operating temperatures of up to 800 °C.

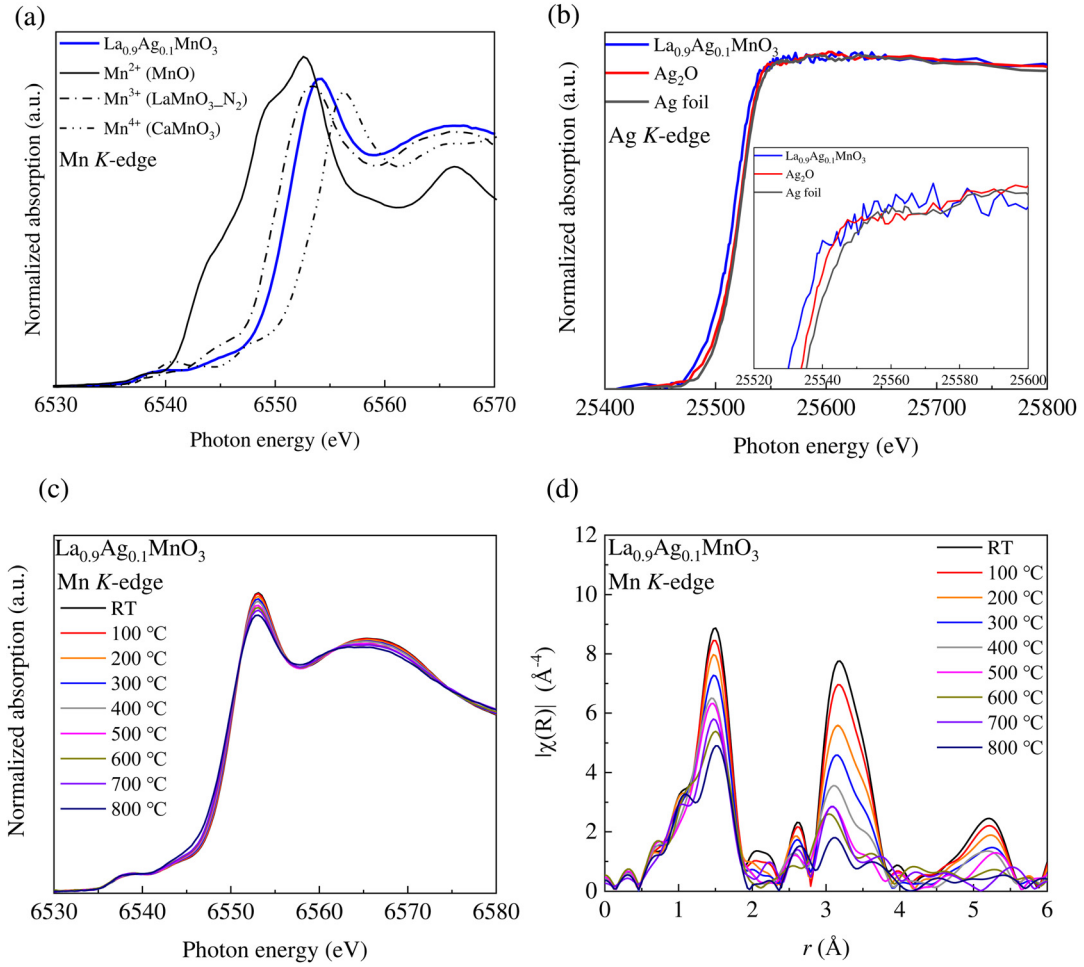

Fig. 4 (a) *Ex situ* Mn K-edge XANES spectra, (b) *ex situ* Ag K-edge XANES spectra of LAM01 at room temperature. (c) *in situ* Mn K-edge XANES spectra and (d) amplitude of Fourier transformed obtained from EXAFS oscillation of LAM01 from room temperature to 800 °C in air. The weighted spectra were Fourier transformed in a *k* space of 3 to 12 $Å^{-1}$.

3.3 Electrical conductivity and Seebeck coefficient

Fig. 5(a) shows the electrical conductivity, σ, measured in air. The conductivity increased with increasing temperature. The activation energy was 0.170 eV (Fig. S3, ESI†). The relative density of LAM01 was 51%; therefore, the conductivities were calibrated by density correction factors.[47] Ag doped $LaMnO_3$ could be a mixed conductor of ions and electrons, but the high conductivity value suggested that it was mainly an electron conductor. Fig. 5(b) shows the Seebeck coefficients measured in air. The Seebeck coefficient of Sr-doped $LaMnO_3$ measured in 100% O_2 by Mizusaki *et al.* is also plotted as the reference.[43] The Seebeck coefficients were positive, suggesting that the charge carrier was an electron hole. The electronic conductivity measurements suggested electric conduction and the Seebeck coefficient measurements implied that the main charge carrier was the electron–hole.

3.4 Power generation characteristics

The *I–V*/*I–P* curves and impedance spectra of the SOFC cell using the LAM01 cathode, which was baked at 925 °C, are shown in Fig. 6(a). Stable power generation curves were obtained using the LAM01 cathode, indicating that LAM01 is stable and applicable as an SOFC cathode. The impedance of the cathode showed larger resistance than the anode for the measured temperatures, and cathode resistance increased as temperature decreased (Fig. 6(b)). The EDX analysis data after the power generation test showed a slight decrease in the Ag ratio (Table 2). The EDX analysis suggested that the Ag ratio did not change much after annealing at 975 °C (Table 1). Thus, this slight ratio change was attributed to the effect of the Pt current collector because Pt easily reacts with Ag and forms a Pt–Ag alloy and the cathode was baked after the Pt mesh was attached. Therefore, even though LAM01 is stable under annealing in air, when LAM01 is used as a SOFC cathode, the choice of the current collector is important because Ag is removed from the perovskite structure by alloying. In addition, the Ag-doped $LaMnO_3$ cathode baked at 925 °C showed delamination during the power generation test (Fig. 7). There are two possible reasons for the delamination; one is insufficient baking temperature, and the other is the large mismatch between the thermal expansion coefficients (TECs) of LAM01

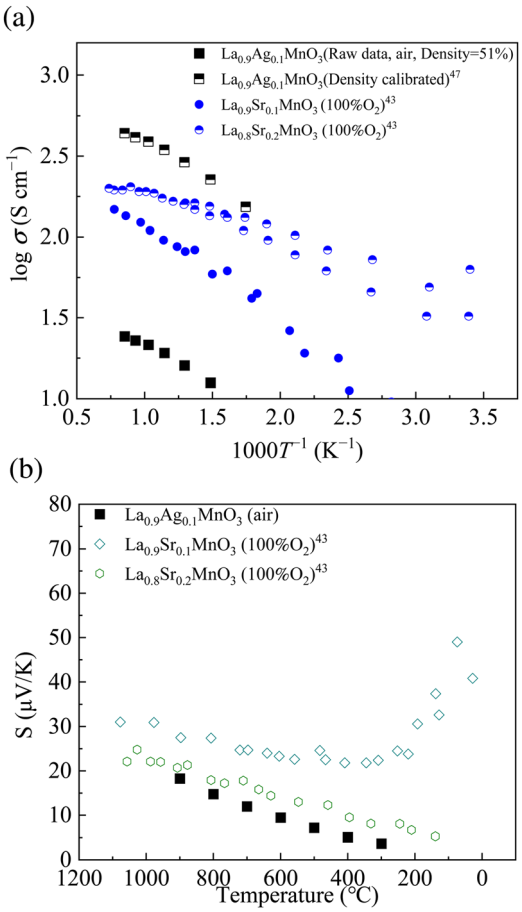

Fig. 5 (a) Electrical conductivity of Ag doped $LaMnO_3$ measured in air. The bulk conductivity of Ag doped $LaMnO_3$ was calibrated by density correction factors.[47] (b) Absolute Seebeck coefficients of Ag doped $LaMnO_3$ measured in air. For comparison, those of LSM measured in 100% O_2 are also shown.[43]

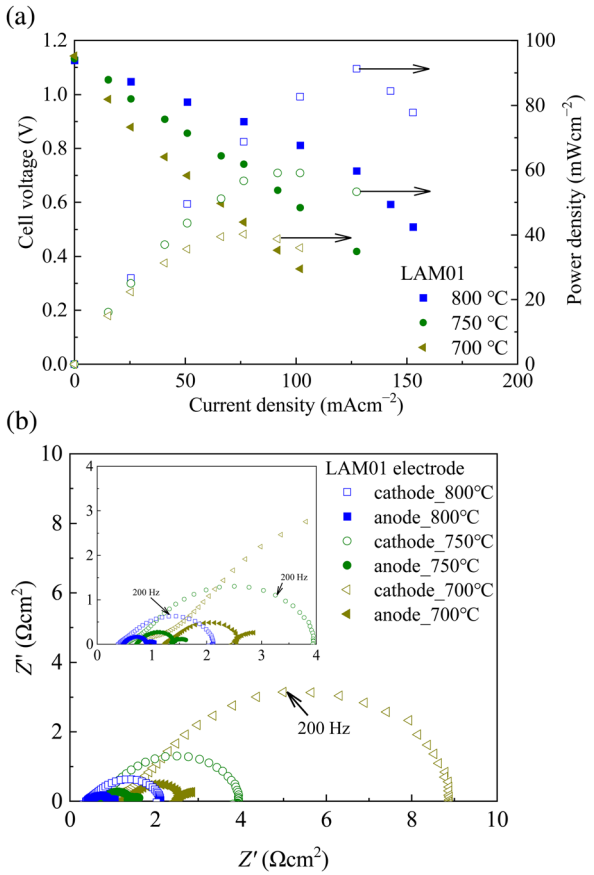

Fig. 6 (a) Power generation characteristic curves and (b) impedance profiles of the LAM01 cell baked at 925 °C.

Table 2 EDX atomic concentrations measured by SEM observations of the LAM01 cathode (baked at 925 °C) after the power generation tests

	La (at %)	Ag (at %)	Mn (at %)
LAM01 cathode (baked at 925 °C)	52.0	2.7	45.3

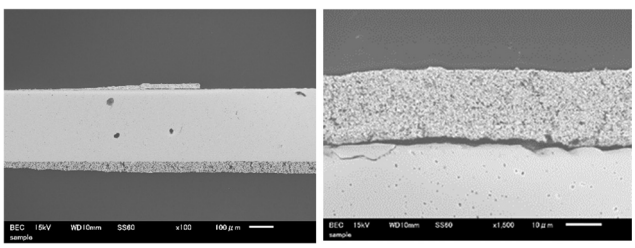

Fig. 7 SEM images after the power generation tests of the LAM01 cell baked at 925 °C (cell cross section).

and YSZ. For example, the TECs of $La_{0.9}Sr_{0.1}MnO_3$ and $La_{0.8}Sr_{0.2}MnO_3$ is 12–13 × 10^{-6} K^{-1}.[48] In addition, it has been reported that TECs do not largely differ depending on the dopant species at lower dopant levels.[49] Thus, we can simply estimate the TEC of LAM01 as 12 to 13 × 10^{-6} K^{-1} from those of $La_{0.9}Sr_{0.1}MnO_3$ and $La_{0.8}Sr_{0.2}MnO_3$, which is very close to that of YSZ (10 × 10^{-6} K^{-1}).[50] Thus, it can be concluded that the main reason for the delamination is the former. To decrease the delamination, we also performed the power generation test using not only the LAM01 cathode baked at 1000 °C but also the LAM01 + YSZ composite cathode baked at 1000 °C (Fig. S4–S6, ESI†). The highest performance of about 220 mW cm^{-2} was obtained at the LAM01 : YSZ ratio of 10 : 0 at 800 °C. Assuming the LAM01 cathode is used with anode support cells (ASCs) and also assuming that the electrolyte resistance of 0.95 Ω cm^2 is subtracted from the total cell resistance since the conductivity of YSZ is $10^{-1.5}$ S cm^{-1} at 800 °C,[7] the power generation density when the ASCs used is estimated to reach about 0.6 W cm^{-2}. Even though the SOFC performance was improved by increasing the baking temperature, the Ag ratio decreased substantially due to alloying (Table S2 and Fig. S2, ESI†). Thus, this result suggests that the choice of cathode baking temperature and an appropriate current collector are important when LAM01 is used as a SOFC cathode. However, the SEM, HAADF-STEM, XPS, SEM-EDX, and XRD results (Fig. S7–S14, ESI†) did not show the deposition of Ag metal and

decomposition of the perovskite structure despite the harsh treatment conditions. That is, the high cathodic performance was unlikely to have been achieved by Ag deposition. In addition, the LAM01 cathode cell baked at 1000 °C showed similar performance to that of the LSM01 cathode, also suggesting that LAM01 may be suitable as an SOFC cathode (Fig. S15, ESI†).

The present results showed that the LAM01 cathode is compatible with a YSZ-based cell. Therefore, Ag is an appropriate acceptor dopant for $LaMnO_3$ cathodes that showed superior compatibility with the YSZ electrolyte and stable cathode performance. From the viewpoint of practical application of SOFC, LAM01 is a promising cathode material. Further improvements *via* introducing a higher concentration of Ag dopant and choosing appropriate cathode fabrication conditions and an appropriate current collector would improve the cathode performance.

4. Conclusions

Ag-doped $LaMnO_3$ was synthesized using a sol–gel method, and its various material properties, including thermodynamic stability against YSZ, which are essential for the SOFC cathode, were investigated and discussed. For 10 mol% Ag doping, Ag was dissolved in $LaMnO_3$ perovskite oxide, whereas 20 mol% Ag doping resulted in the deposition of Ag particles. LAM01 and LAM01 mixed 8YSZ powders were stable at 975 °C for 100 h, showing no change in the crystal structure and confirming material stability at elevated temperatures. LAM01 is an electric conductor in which the main charge carrier is a hole. Power generation tests on 8YSZ electrolyte-supported cells using an LAM01 cathode showed stable cathode properties. Even though problems including determining the cathode baking conditions and choice of the current collector remain, the Ag acceptor is a stable and compatible element with the YSZ electrolyte and Ag-doped $LaMnO_3$ is a promising material for SOFC cathodes. It is expected that high cathode performance can be achieved by resolving these problems.

Data availability

The data supporting the findings of this work are available within the article and supporting information. Raw data that support the findings of this work are available from the corresponding authors (M. O. and T. S.), upon reasonable request.

Conflicts of interest

There are no conflicts to declare.

Acknowledgements

This work was partly supported by Toyota Mobility Foundation (T. M. F.). We thank Mr Tomoyuki Ueki, Tokushima University, for the XPS measurements. We also thank Prof. Ken-ichiro Murai, Tokushima University, for the XRD measurements. X-ray absorption spectroscopy measurements were conducted at SPring-8 under proposal no. 2020A1359 and 2022B1247. This work was also partly supported by Tokushima International Science Office (TISI).

References

1 X.-D. Zhou and S. C. Singhal, Fuel cells – solid oxide fuel cells overview, *Encycl. Electrochem. Power Sources*, 2009, 1–16.
2 N. Q. Minh, Solid oxide fuel cell technology - features and applications, *Solid State Ionics*, 2004, **174**, 271–277.
3 T. Kabata, Development of SOFC triple combined cycle system, *J. Hydrogen Energy Syst. Soc. Jpn*, 2012, **37**, 128–131.
4 S. C. Singhal and K. Kendal, *High temperature and solid oxide fuel cells*, Elsevier Science, Amsterdam, 2003.
5 J. T. S. Irvine, D. Neagu, M. C. Verbraeken, C. Chatzichristodoulou, C. Graves and M. B. Mogensen, Evolution of the electrochemical interface in high temperature fuel cells and electrolysers, *Nat. Energy*, 2016, **1**, 15014.
6 E. C. Subbarao, *Solid electrolytes and their applications*, Plenum Press, New York, 1980.
7 J.-H. Park and R. N. Blumenthal, Electronic transport in 8 mole percent Y_2O_3–ZrO_2, *J. Electrochem. Soc.*, 1989, **136**, 2867–2876.
8 D. W. Stricker and W. G. Carlson, Electrical conductivity in the ZrO_2-rich region of several M_2O_3-ZrO_2 systems, *J. Am. Ceram. Soc.*, 1965, **48**, 286–289.
9 T. Nakamura, M. Misona and Y. Yoneda, Reduction-oxidation and catalytic properties of $La_{1-x}Sr_xCoO_3$, *J. Catal.*, 1983, **83**, 151–159.
10 J. Mizusaki, Y. Mima, S. Yamauchi, K. Fueki and H. Tagawa, Nonstoichiometry of the perovskite-type oxides $La_{1-x}Sr_xCoO_{3-\delta}$, *J. Solid State Chem.*, 1989, **80**, 102–111.
11 Y. Orikasa, T. Ina, T. Nakao, A. Mineshige, K. Amezawa, M. Oishi, H. Arai, Z. Ogumi and Y. Uchimoto, X-ray absorption spectroscopic study on La0.6Sr0.4CoO3−δ cathode materials related with oxygen vacancy formation, *J. Phys. Chem. C*, 2011, **115**, 16433–16438.
12 S. B. Adler, Mechanism and kinetics of oxygen reduction on porous $La_{1-x}Sr_xCoO_{3-\delta}$ electrodes, *Solid State Ionics*, 1998, **111**, 125–134.
13 Y. Takeda, R. Kanno, M. Noda, Y. Tomida and O. Yamamoto, Cathodic polarization phenomena of perovskite oxide electrodes with stabilized zirconia, *J. Electrochem. Soc.*, 1987, **134**, 2656–2661.
14 Y. Choi, D. S. Mebane, M. C. Lin and M. Liu, Oxygen reduction on $LaMnO_3$-based cathode materials in solid oxide fuel cells, *Chem. Mater.*, 2007, **19**, 1690–1699.
15 J. H. Kuo, H. U. Anderson and D. M. Spalin, Oxidation-reduction behavior of undoped and Sr-doped LaMnO3: Defect structure, electrical conductivity, and thermoelectric power, *J. Solid State Chem.*, 1990, **87**, 55–63.
16 L.-W. Tai, M. M. Nasrallah, H. U. Anderson, D. M. Sparln and S. R. Sehlin, Structure and electrical properties of

$La_{1-x}Sr_xCo_{1-y}Fe_yO_3$, Part 1. The system $La_{0.8}Sr_{0.2}Co_{1-y}Fe_yO_3$, *Solid State Ionics*, 1995, **76**, 259–271.

17 L.-W. Tai, M. M. Nasrallah, H. U. Anderson, D. M. Sparln and S. R. Sehlin, Structure and electrical properties of $La_{1-x}Sr_xCo_{1-y}Fe_yO_3$, Part 2. The system $La_{1-x}Sr_xCo_{0.2}Fe_{0.8}O_3$, *Solid State Ionics*, 1995, **76**, 273–283.

18 M. Kuhn, Y. Fukuda, S. Hashimoto, K. Sato, K. Yashiro and J. Mizusaki, Oxygen nonstoichiometry and thermo-chemical stability of perovskite-type $La_{0.6}Sr_{0.4}Co_{1-y}FeyO_{3-\delta}$ (y = 0, 0.2, 0.4, 0.5, 0.6, 0.8, 1) materials, *J. Electrochem. Soc.*, 2013, **160**, F34–F42.

19 Y. Orikasa, T. Ina, T. Nakao, A. Mineshige, K. Amezawa, M. Oishi, H. Arai, Z. Ogumi and Y. Uchimoto, An X-ray absorption spectroscopic study on mixed conductive $La_{0.6}Sr_{0.4}Co_{0.8}Fe_{0.2}O_{3-\delta}$ cathodes. I. Electrical conductivity and electronic structure, *Phys. Chem. Chem. Phys.*, 2011, **13**, 16637–16643.

20 L. Kindermann, D. Das, H. Nickel and K. Hilpert, Chemical compatibility of the $LaFeO_3$ base perovskites, $(La_{0.6}Sr_{0.4})zFe_{0.8}M_{0.2}O_{3-\delta}$, ($Z$ = 1, 0.9; M = Cr, Mn, Co, Ni) with yttria stabilized zirconia, *Solid State Ionics*, 1996, **89**, 215–220.

21 H. Yokokawa, N. Sakai, T. Kawada and M. Dokiya, Chemical thermodynamic consideration on reactivity of perovskite oxide electrodes with zirconia, *Denki Kagaku*, 1989, **57**, 821–828.

22 M. Sase, D. Ueno, K. Yashiro, A. Kaimai, T. Kawada and J. Mizusaki, Interfacial reaction and electrochemical properties of dense $(La,Sr)CoO_{3-\delta}$ cathode on YSZ (1 0 0), *J. Phys. Chem. Solids*, 2005, **66**, 343–348.

23 J. Mizusaki, H. Tagawa, K. Tsuneyoshi, K. Mori and A. Sawata, Electrode thickness, microstructure, and properties of air electrode for high-temperature solid oxide fuel cells, $La_{0.6}Ca_{0.4}MO_3$ (M = Mn,Co)/YSZ, *Nippon Kagaku Kaishi*, 1988, **9**, 1623–1629.

24 J.-T. Chou, Y. Inoue, T. Kawabata, J. Matsuda, S. Taniguchi and K. Sasaki, Mechanism of $SrZrO_3$ formation at GDC/YSZ interface of SOFC cathode, *J. Electrochem. Soc.*, 2018, **165**(11), F959–F965.

25 H. Naito, N. Sakai, T. Otake, H. Yugami and H. Yokokawa, Oxygen transport properties in ZrO_2–CeO_2–Y_2O_3 by SIMS analysis, *Solid State Ionics*, 2000, **135**, 669.

26 M. Chen, Y.-L. Liu, A. Hagen, P. V. Hendriksen and F. W. Poulsen, LSM-YSZ reactions in different atmospheres, *Fuel Cells*, 2009, **9**(6), 833–840.

27 Y. L. Liu, A. Hagen, R. Barfod, M. Chen, H. J. Wang, F. W. Poulsen and P. V. Hendriksen, Microstructural studies on degradation of interface between LSM-YSZ cathode and YSZ electrolyte in SOFCs, *Solid State Ionics*, 2009, **180**, 1298–1304.

28 Y. Takeda, Y. Sakaki, T. Ichikawa, N. Imanishi, O. Yamamoto, M. Mori, N. Mori and T. Abe, Stability of $La_{1-x}A_xMnO_{3-z}$ (A = Ca, Sr) as cathode materials for solid oxide fuel cells, *Solid State Ionics*, 1994, **72**, 257–264.

29 Y. Kalyana Lakshmi, N. Pavan Kumar and P. Venugopal Reddy, Thermopower studies of polycrystalline Ag doped $LaMnO_3$ Manganites, *J. Supercond. Nov. Magn.*, 2013, **26**, 2975–2980.

30 M. B. Bellakki, C. Shivakumara, N. Y. Vasanthacharya and A. S. Prakash, Rapid synthesis of room temperature ferromagnetic Ag-doped $LaMnO_3$ perovskite phases by the solution combustion method, *Mater. Res. Bull.*, 2010, **45**, 1685–1691.

31 R. Sažinas, K. B. Andersen, S. B. Simonsen, P. Holtappels and K. K. Hansen, Silver modified cathodes for solid oxide fuel cells, *J. Electrochem. Soc.*, 2019, **166**(2), F79–F88.

32 S. P. Simner, M. D. Anderson, J. W. Templeton and J. W. Stevenson, Silver-perovskite composite SOFC cathodes processed via mechanofusion, *J. Power Sources*, 2007, **168**, 236–239.

33 Z. Wang and M. Mori, SOFC-SOEC Characteristics of an intermediate-temperature micro-tubular ceramic reactor using Ag for current collecting, *Electrochemistry*, 2010, **78**(7), 601–605.

34 Y. Liu, S. Hashimoto, K. Yasumoto, K. Takei, M. Mori, Y. Funahashi, Y. Fijishiro, A. Hirano and Y. Takeda, Preparation and application of nano-dispersed Ag in $La_{0.6}Sr_{0.4}Co_xFe_{1-x}O_{3-d}$ perovskites for intermediate-temperature solid oxide fuel cell, *Curr. Appl. Phys.*, 2009, **9**, S51–S53.

35 J. H. Kim, J. K. Kim, H. G. Seo, D.-K. Lim, S. J. Jeong, J. Seo, J. Kim and W. C. Jung, Ex-solved Ag nanocatalysts on a Sr-free parent scaffold authorize a highly efficient route of oxygen reduction, *Adv. Funct. Mater.*, 2020, **30**(27), 2001326.

36 T. Sakai, M. Ogushi, K. Hosoi, A. Inoishi, S. Ida, M. Oishi and T. Ishihara, Characteristics of $YCoO_3$-type perovskite oxide and application as an SOFC cathode, *J. Mater. Chem. A*, 2021, **9**, 3584–3588.

37 T. Uruga, H. Tanida, Y. Yoneda, K. Takeshita, S. Emura and M. Takahashi, The XAFS beamline BL01B1 at SPring-8, *J. Synchrotron Radiat.*, 1999, **6**, 143–145.

38 T. Taguchi, J. Harada, A. Kiku, K. Tohji and K. Shinoda, Development of a new in-laboratory XAFS apparatus based on new concept, *J. Synchrotron Radiat.*, 2001, **8**, 363–365.

39 B. Ravel and M. Newville, ATHENA, ARTEMIS, HEPHAESTUS: data analysis for X-ray absorption spectroscopy using IFEFFIT, *J. Synchrotron Radiat.*, 2005, **12**, 537–541.

40 T. Yamamoto, S. Mori, T. Kawaguchi, T. Tanaka, K. Nakanishi, T. Ohta and J. Kawai, Evidence of a strained pore wall structure in mesoporous silica FSM-16 studied by X-ray absorption spectroscopy, *J. Phys. Chem. C*, 2008, **112**, 328–331.

41 N. Cusack and P. Kendall, The absolute scale of thermoelectric power at high temperature, *Proc. Phys. Soc.*, 1958, **72**, 898–901.

42 T. Nakamura, K. Yashiro, K. Sato and J. Mizusaki, Electronic state of oxygen nonstoichiometric $La_{2-x}Sr_xNiO_{4+\delta}$ at high temperatures, *Phys. Chem. Chem. Phys.*, 2009, **11**, 3055–3062.

43 J. Mizusaki, N. Mori, H. Takai, Y. Yonemura, H. Minamiue, H. Tagawa, M. Dokiya, H. Inaba, K. Naraya, T. Sasamoto and T. Hashimoto, Oxygen nonstoichiometry and defect

equilibrium in the perovskite-type oxides $La_{1-x}Sr_xMnO_{3+\delta}$, *Solid State Ionics*, 2000, **129**, 163–177.

44 B. A. Manning, S. R. Kanel, E. Guzman, S. W. Brittle and I. E. Pavel, Oxidative dissolution of silver nanoparticles by synthetic manganese dioxide investigated by synchrotron X-ray absorption spectroscopy, *J. Nanopart. Res.*, 2019, **21**(213), 1–15.

45 I. J. Godfrey, A. J. Dent, I. P. Parkin, S. Maenosono and G. Sankar, Structure of Gold−Silver Nanoparticles, *J. Phys. Chem. C*, 2017, **121**, 1957–1963.

46 L. Wang, T. Zhang, P. Li, W. Huang, J. Tang, P. Wang, J. Liu, Q. Yuan, R. Bai, B. Li, K. Zhang, Y. Zhao and C. Chen, Use of Synchrotron Radiation-Analytical Techniques To Reveal Chemical Origin of Silver-Nanoparticle Cytotoxicity, *ACS Nano*, 2015, **6**, 6532–6547.

47 H. Tagawa, J. Mizusaki, Y. Arai, Y. Kuwayama, S. Tsuchiya, T. Takeda and S. Sekido, Sinterability and electrical conductivity of variously prepared perovskite-type oxide, $La_{0.5}Sr_{0.5}CoO_3$, *Denki Kagaku*, 1990, **58**(6), 512–519.

48 H. Inaba and H. Tagawa, Semi-Empirical Estimation of Thermal Expansion Coefficients of Perovskite-Type Oxide, *J. Ceram. Soc. Jpn.*, 1998, **106**(3), 272–278.

49 J. Mastin, M.-A. Einarsrud and T. Grande, Structural and Thermal Properties of $La_{1-x}Sr_xCoO_{3-\delta}$, *Chem. Mater.*, 2006, **18**, 6047–6053.

50 T. Kawashima and M. Hishinuma, Thermal Expansion Coefficient and Residual Stress of Porous Ni/ZrO_2–Y_2O_3 Cermet, *J. Ceram. Soc. Jpn.*, 1998, **106**(7), 682–687.